Quantifying dwarf satellites through gravitational imaging

Vegetti, Simona; Czoske, Oliver; Koopmans, Léon V. E.

Published in:
Monthly Notices of the Royal Astronomical Society

DOI:
10.1111/j.1365-2966.2010.16952.x

Publication date:
2010

Monthly Notices
of the
ROYAL ASTRONOMICAL SOCIETY

Mon. Not. R. Astron. Soc. **407,** 225–231 (2010) doi:10.1111/j.1365-2966.2010.16952.x

Quantifying dwarf satellites through gravitational imaging: the case of SDSS J120602.09+514229.5

Simona Vegetti,★ Oliver Czoske† and Léon V. E. Koopmans

Kapteyn Astronomical Institute, University of Groningen, PO Box 800, 9700 AV Groningen, the Netherlands

Accepted 2010 May 2. Received 2010 April 23; in original form 2010 February 22

ABSTRACT

SDSS J120602.09+514229.5 is a gravitational lens system formed by a group of galaxies at redshift $z_{\rm FG} = 0.422$ lensing a bright background galaxy at redshift $z_{\rm BG} = 2.001$. The main peculiarity of this system is the presence of a luminous satellite near the Einstein radius, which slightly deforms the giant arc. This makes SDSS J120602.09+514229.5 the ideal system to test our grid-based Bayesian lens modelling method, designed to detect Galaxy satellites independently of their mass-to-light ratio and to measure the mass of this dwarf galaxy despite its high redshift. We model the main lensing potential with a composite analytical density profile consisting of a single power law for the group dominant galaxy and two singular isothermal spheres for the other two group members. Thanks to the pixelized source and potential reconstruction technique of Vegetti and Koopmans, we are able to detect the luminous satellite as a local positive surface density correction to the overall smooth mass model. Assuming a truncated pseudo-Jaffe density profile, the satellite has a mass $M_{\rm sub} = (2.75 \pm 0.04) \times 10^{10}\,{\rm M}_{\odot}$ inside its tidal radius of $r_{\rm t} = 0.68$ arcsec. This result is robust against changes in the lens model. We determine for the satellite a luminosity of $L_B = (1.6 \pm 0.8) \times 10^9\,{\rm L}_{\odot}$, leading to a total mass-to-light ratio within the tidal radius of $(M/L)_B = (17.2 \pm 8.5)\,{\rm M}_{\odot}/{\rm L}_{\odot}$. The central galaxy has a sub-isothermal density profile as in general is expected for group members. From the Sloan Digital Sky Survey (SDSS) spectrum, we derive for the central galaxy a velocity dispersion of $\sigma_{\rm kinem} = 380 \pm 60\,{\rm km\,s^{-1}}$ within the SDSS aperture of a diameter of 3 arcsec. The logarithmic density slope of $\gamma = 1.7^{+0.25}_{-0.30}$ [68 per cent confidence limit (CL)], derived from this measurement, is consistent within 1σ with the density slope of the dominant lens galaxy $\gamma \approx 1.6$ determined from the lens model. This paper shows how powerful pixelized lensing techniques are in detecting and constraining the properties of dwarf satellites at high redshift.

Key words: gravitational lensing: strong – galaxies: dwarf – galaxies: groups: general – galaxies: haloes – galaxies: structure – dark matter.

1 INTRODUCTION

Comparison between numerical cold dark matter (CDM) simulations and direct observations of the Milky Way and Andromeda has shown the existence of a strong discrepancy in which the abundance of predicted subhaloes outnumbers that of observed dwarf galaxies (e.g. Kauffmann, White & Guiderdoni 1993; Klypin et al. 1999; Springel et al. 2008; Kravtsov 2010, and references therein). Reconciling the luminosity function with the mass function is therefore a crucial test for CDM models. With the specific aim of addressing this issue, a grid-based Bayesian lens modelling code was developed by Vegetti & Koopmans (2009a). This technique is able to identify possible mass substructure in the lensing potential, by reconstructing the surface brightness distribution of lensed arcs and Einstein rings. Several tests on mock data have shown that we can detect mass substructure as massive as $M_{\rm sub} \geq 10^8\,{\rm M}_{\odot}$ (Vegetti & Koopmans 2009a,b).

In a recent application to the lens system SDSS J0946+1006 from the Sloan Lens ACS Survey (Bolton et al. 2006), the method has proved to be successful in recovering the smooth lensing potential and in identifying a satellite with a high mass-to-light ratio $(M/L)_{\rm V} \gtrsim 120 (M/L)_{\rm V,\odot}$ and with mass $M_{\rm sub} \sim (3.51 \pm 0.15) \times 10^9\,{\rm M}_{\odot}$, while reconstructing the data to the noise level (Vegetti et al. 2009). However, the complexity of the data and systematic effects related for example to sub-pixel structure, point spread function (PSF) modelling and spatially varying noise can complicate the source and the potential reconstruction, and all their effects

★E-mail: vegetti@astro.rug.nl

†Current address: Institut für Astronomie, Türkenschanzstr. 17, A-1180 Wien, Austria.

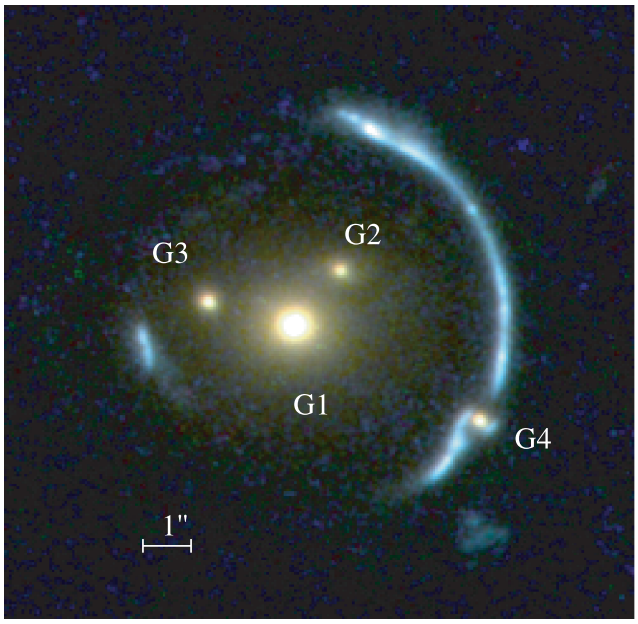

Figure 1. Overview of the lens system SDSS J120602.09+514229.5. This false-colour image was created from *HST*/WFPC2 images in F450W, F606W and F814W.

always have to be carefully assessed and quantified. A definitive test is therefore required to *calibrate* the capability of our technique. SDSS J120602.09+514229.5 (Lin et al. 2009) with a luminous satellite right on the lensed images (see Fig. 1) is an ideal system to accomplish this task. In this paper we present a full analysis of SDSS J120602.09+514229.5, measuring the mass and the mass-to-light-ratio of the dwarf satellite and showing the strength of the method on known satellites. The layout of the paper is as follows. In Section 2, we introduce the data. In Section 3 we provide a short description of the modelling method and a detailed description of the main results, and in Section 4 we summarize our main results. Throughout the paper, we assume the following cosmology: $H_0 = 73\,\mathrm{km\,s^{-1}\,Mpc^{-1}}$, $\Omega_\mathrm{m} = 0.25$ and $\Omega_\Lambda = 0.75$.

2 THE DATA

SDSS J120602.09+514229.5 (the Clone) was observed with the *Hubble Space Telescope* (*HST*) in cycle 16 (P.I.: S. Allam). Wide Field Planetary Camera 2 (WFPC2) images were obtained through three filters: F450W, F606W and F814W. We base our lens model on the F606W data because they provide the best combination of depth and resolution.

Four dithered exposures were obtained, each with an integration time of 1100 s. We retrieved the calibrated exposures from the *HST* archive and used *multidrizzle* to combine them. The final image has a pixel scale of 0.05 arcsec.

To model the observed structure of the lensed source, we require knowledge of the PSF of the drizzled image. Since there are no suitable stars in the field, we rely on a model PSF created with Tiny Tim, v6.3 (Krist 1993).[1] The PSF is generated for the position of the lens system on chip 2 of the WFPC2, subsampled by a factor of 10. Subsampling is necessary because the dither pattern involves half-pixel shifts which cannot be taken into account by Tiny Tim alone. Instead we rebin the highly subsampled PSF to the original WFPC2 pixel scale once for each science exposure, with the output grid shifted by 5 subsampled pixels to account for half-pixel shifts. The rebinned PSF is inserted at the position of the lens galaxy G1 in copies of the four science files after setting the image data to zero. These PSF exposures are then drizzled with the same parameters as before to create an approximation to the PSF of the drizzled science image.

Light from the outer parts of the main lens galaxies G1, G2 and G3 contributes a few per cent to the light at the location of the lensed arc images. We subtract de Vaucouleur models of these galaxies, generated with GALFIT,[2] version 3.0 (Peng et al. 2002). The effective radius of G1 is determined at 3.9 ± 0.1 arcsec.

Finally, we need to remove the satellite galaxy G4. Since this galaxy sits on top of an arc image and it is not a priori clear what the background level due to light from the arc is, no unambiguous model of G4 can be determined. Due to its compactness, we opt to subtract a simple Gaussian model with a full width at half-maximum of 0.173 arcsec and normalization determined from visual impression of the image after subtraction. Changes in the normalization within a plausible range do not significantly affect the potential reconstruction.

A spectrum of G1 is available from the Sloan Digital Sky Survey (SDSS). This spectrum has a fairly low signal-to-noise ratio (S/N) of $\approx$8 (per pixel), and no kinematic measurements are given in the SDSS data base. With the template fitting method described in Czoske et al. (in preparation; see also Czoske et al. 2008) and the Indo-US spectrum (Valdes et al. 2004) of the K2III star HD 195506 as a template we obtain a good fit (reduced $\chi^2 = 1.11$; Fig. 2) with a velocity dispersion of $\sigma_\mathrm{kinem} = 380 \pm 60\,\mathrm{km\,s^{-1}}$ within the SDSS aperture of a diameter of 3 arcsec. This is lower than but not inconsistent with the value that Lin et al. (2009) obtained from fitting a singular isothermal ellipsoid (SIE) model to the lens configuration, $\sigma_\mathrm{SIE} = 440 \pm 7\,\mathrm{km\,s^{-1}}$. Note, however, that this value applies to the entire mass doing the lensing, whereas our value is for the main lens galaxy G1 only.

3 LENS MODELLING

The lens modelling is performed using the Bayesian adaptive method of Vegetti & Koopmans (2009a) to which we refer for a detailed description. Briefly, we proceed as follows.

(i) Initially, we only assume a smooth analytic model for the main lens potential (i.e. we only consider G1, G2 and G3) and maximize the relative posterior probability in terms of their lens parameters. At this point, we ignore the satellite G4.

(ii) We fix the lens potential at the maximum posterior values found in the previous iteration and perform a simultaneous pixelized reconstruction of the source surface brightness distribution $\boldsymbol{s}$ and the potential correction $\delta\boldsymbol{\psi}$. This leads to the detection and localization of possibly present mass substructures in the lens potential.

(iii) Finally, we build a composite analytic model in which both the main lenses and the detected satellite have a power-law (PL) density profile and we optimize the relative penalty function for the corresponding parameters. The PL is truncated in the case of the satellite.

In the next sections, we describe this procedure in more detail as applied to the lens SDSS J120602.09+514229.5, and show that it is able to detect and quantify the satellite G4.

[1] http://www.stsci.edu/software/tinytim/tinytim.html

[2] http://users.obs.carnegiescience.edu/peng/work/galfit/galfit.html

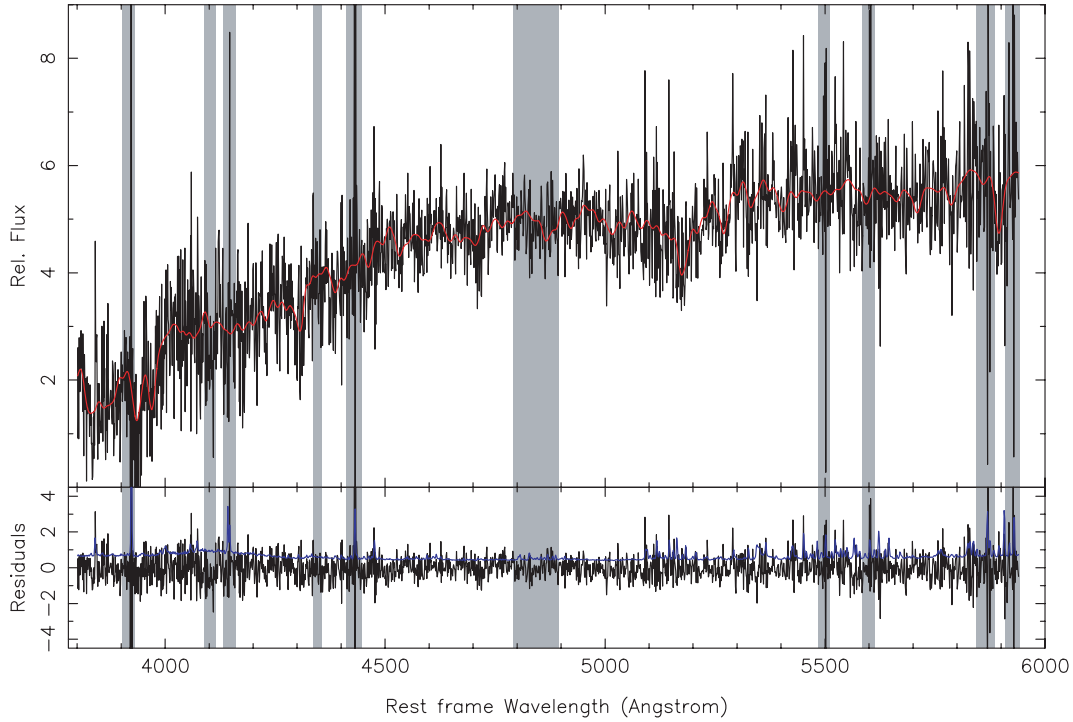

Figure 2. SDSS spectrum of galaxy G1 is shown in the upper panel. The spectrum of K2III star HD 195506 is convolved with a Gaussian line-of-sight velocity distribution of a dispersion of 380 km s^{-1} overlaid in red. The residuals of the fit are plotted in the lower panel, with the expected noise spectrum overlaid in blue. The masked regions are for Balmer lines, metal lines that typically show abundance anomalies compared to Galactic template spectra, atmospheric absorption features and regions that appear contaminated with strong spikes.

3.1 Smooth potential parametric reconstruction

We initially start with a smooth model that explicitly excludes the satellite G4. We model the lensing potential as the combination of a single PL ellipsoid for G1 and two singular isothermal spheres (SIS) for G2 and G3 with a surface density in terms of critical density Σ_c (Kormann, Schneider & Bartelmann 1994):

$$\Sigma(r) = \frac{\Sigma_c\, b}{2\sqrt{q}\, r^{\gamma-1}}, \qquad (1)$$

where $r = \sqrt{x^2 + y^2/q^2}$.

Given the relatively high dynamic range of the lensed image surface brightness distribution, the source is reconstructed on a Delaunay tessellation grid that is built from the image plane by casting every second pixel in right ascension and declination back to the source plane. The area of each triangle (i.e. the grid resolution) depends on the local lens magnification. A curvature source regularization is adopted (Vegetti & Koopmans 2009a). The free parameters for the posterior probability maximization are the lens strength b, the position angle θ, the axial ratio q and the density slope γ for G1, the lens strength for G2 and G3, the strength of the external shear Γ_{sh} and its position angle θ_{sh}. The best PL+2SIS model is reported in Table 1. We find that this is an incomplete and simplified description for the true lensing potential of SDSS J120602.09+514229.5 and do not expect it to provide a good description of the data. It does, however, provide a sufficient starting point for the next

Table 1. Best recovered parameters for the mass model distribution for the lens SDSS J120602.09+514229.5. For each of the considered models, we report the best recovered set of non-linear parameters and the galaxy centroids.

Model	Lens	b/M_{sub}	θ (deg)	q	x_c (arcsec)	y_c (arcsec)	γ	Γ_{sh}	θ_{sh} (deg)	log L
PL+2SIS	G1	1.59	−50.7	0.75	−0.54	−0.13	1.48	−0.06	−27.8	48 956.90
	G2	0.54		≡1.00	0.38	−0.98	≡2.0			
	G3	0.55		≡1.00	−2.23	0.33	≡2.0			
SIE	G1+G2+G3	3.67	−71.2	0.76	−0.45	0.002	≡2.0	0.005	−63.1	50 267.43
PL+2SIS+PJ	G1	2.27	−79.2	0.80	−0.54	−0.13	1.58	0.03	3.53	102 308.08
	G2	0.17		≡1.00	0.38	−0.98	≡2.0			
	G3	0.13		≡1.00	−2.23	0.33	≡2.0			
	G4	2.78×10^{10} M$_\odot$			3.12	−2.10				
SIE+PJ	G1+G2+G3	3.78	−74.7	0.80	−0.45	0.002	≡2.0	0.02	−74.1	114 035.73
	G4	2.75×10^{10} M$_\odot$			3.12	−2.10				

modelling step. Following Lin et al. (2009), we also tried a simplified model where the lensing potential of G1, G2 and G3 is described by a single global SIE (plus external shear), with free parameters being b, θ, q, the centroid coordinates x_c and y_c, Γ_{sh} and θ_{sh} (see Table 1). For this model, our results are consistent with Lin et al. (2009) but still provide an approximate description of the lens data. Assuming the total mass inside the Einstein radius and the SDSS luminosity-weighted stellar velocity dispersion as two independent constraints, we determine an effective logarithmic density slope, based on spherical Jeans modelling (see Koopmans et al. 2006 for details), of $\gamma = 1.7^{+0.25}_{-0.30}$ (68 per cent confidence limit (CL)), assuming orbital isotropy ($\beta = 0$), an effective radius of 3.9 ± 0.1 arcsec for G1 and a seeing of 1.5 arcsec. Conversely, the best PL density slope of G1, i.e. $\gamma = 1.6$, predicts a dispersion of 340 km s^{-1}. Hence, the best PL model is in excellent agreement with the measured stellar velocity dispersion, although the SIE model, which predicts a large dispersion of 450 km s^{-1}, is still marginally in agreement given the larger error on its measured value.

3.2 Satellite detection

The next step is to test whether the pixelized technique is able to identify the satellite G4. We fix the lens parameters of G1, G2 and G3 to the values found in the previous section and perform a linearized grid-based reconstruction for the source surface brightness and lens potential corrections. To ensure the linearity of the solution, both the source and the potential corrections are initially over-regularized and then the relative regularization constants are slowly lowered. Curvature regularization is used for both the source $\boldsymbol{s}$ and potential corrections $\delta\boldsymbol{\psi}$.

The potential corrections are reconstructed on a regular Cartesian grid with 81 × 81 pixels and a pixel scale of 0.12 arcsec. Via the Poisson equation $\delta\boldsymbol{\psi}$ can be translated into convergence (surface density) corrections $\delta\boldsymbol{\kappa} = \frac{1}{2}(\delta\psi_{11} + \delta\psi_{22})$. A strong positive convergence correction is found at the exact position of G4 (see Fig. 3). Smooth non-negligible density corrections are also found on the upper side of the arc. These could be related to the fact that the source regularization is not at its optimal level, but slightly over-regularized, or is more likely to smooth deviations of the starting model from the true mass distribution (see e.g. Barnabè et al. 2009). We note here that Lin et al. (2009) found non-negligible image residuals near the upper part of the arc. We find that these residuals are predominantly the result of the absence of G4 in their lens model, which affects the structure of the entire arc and leads to a very poor model for its surface brightness distribution, as indicated by the very large difference in likelihood between mass models that include or exclude G4. The iterative potential correction effectively reduces these image residuals to the noise level (see Figs 3 and 4), resulting in the mass reconstruction of G4 *and* the non-negligible density corrections on the upper part of the arc, as discussed above. Neither of these structures have been inferred by Lin et al. (2009). Because the mass distribution of this group is unlikely a sum of three (or four) smooth elliptical PL models, we think that the density structure near the upper part of the arc is genuine and is due

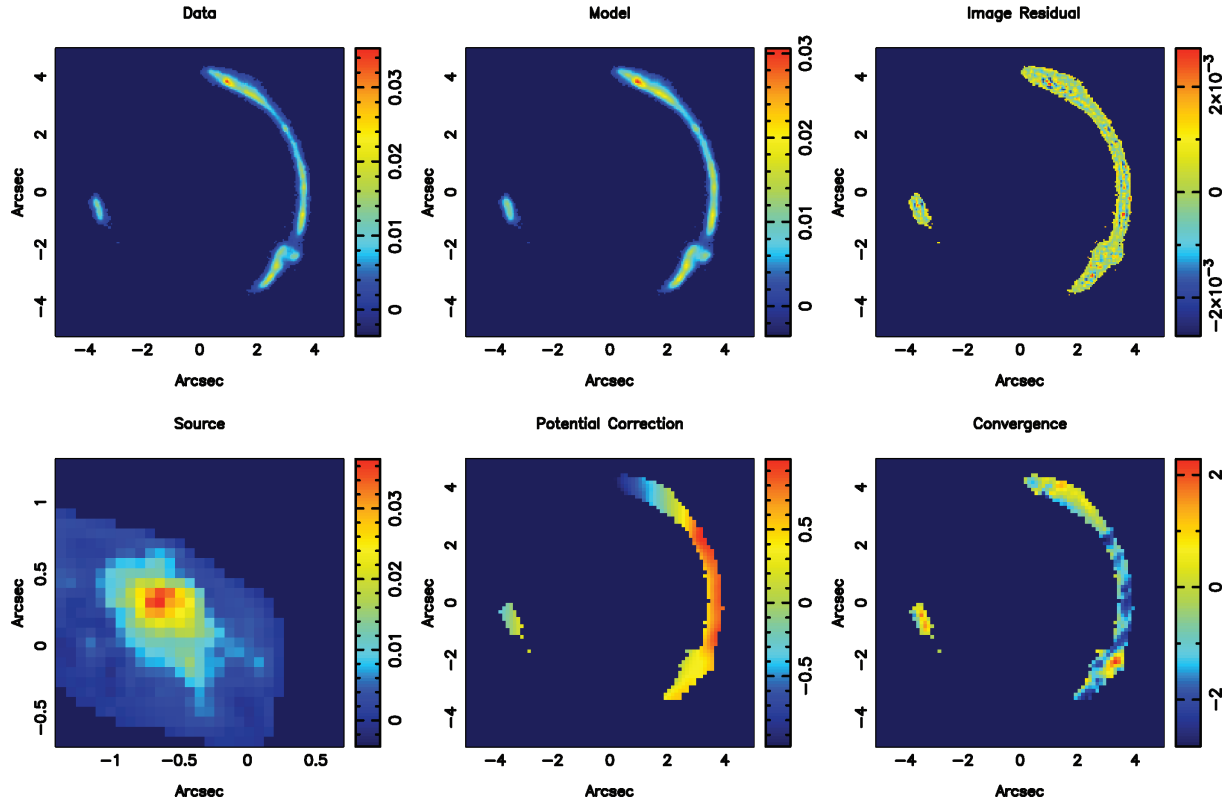

Figure 3. Results of the pixelized reconstruction of the source and lens potential corrections. The top-left panel shows the original lens data, the middle one shows final reconstruction while the top-right one shows the image residuals. On the second row, the source reconstruction (left), the potential correction (middle) and the potential correction convergence (right) are shown. The units for the surface brightness maps (i.e. data, model and source) and residual map (i.e. data minus model) are arbitrary. The convergence is in critical-density units, whereas the potential correction has units of critical-density times square arcseconds and is related to the convergence through the Poisson equation.

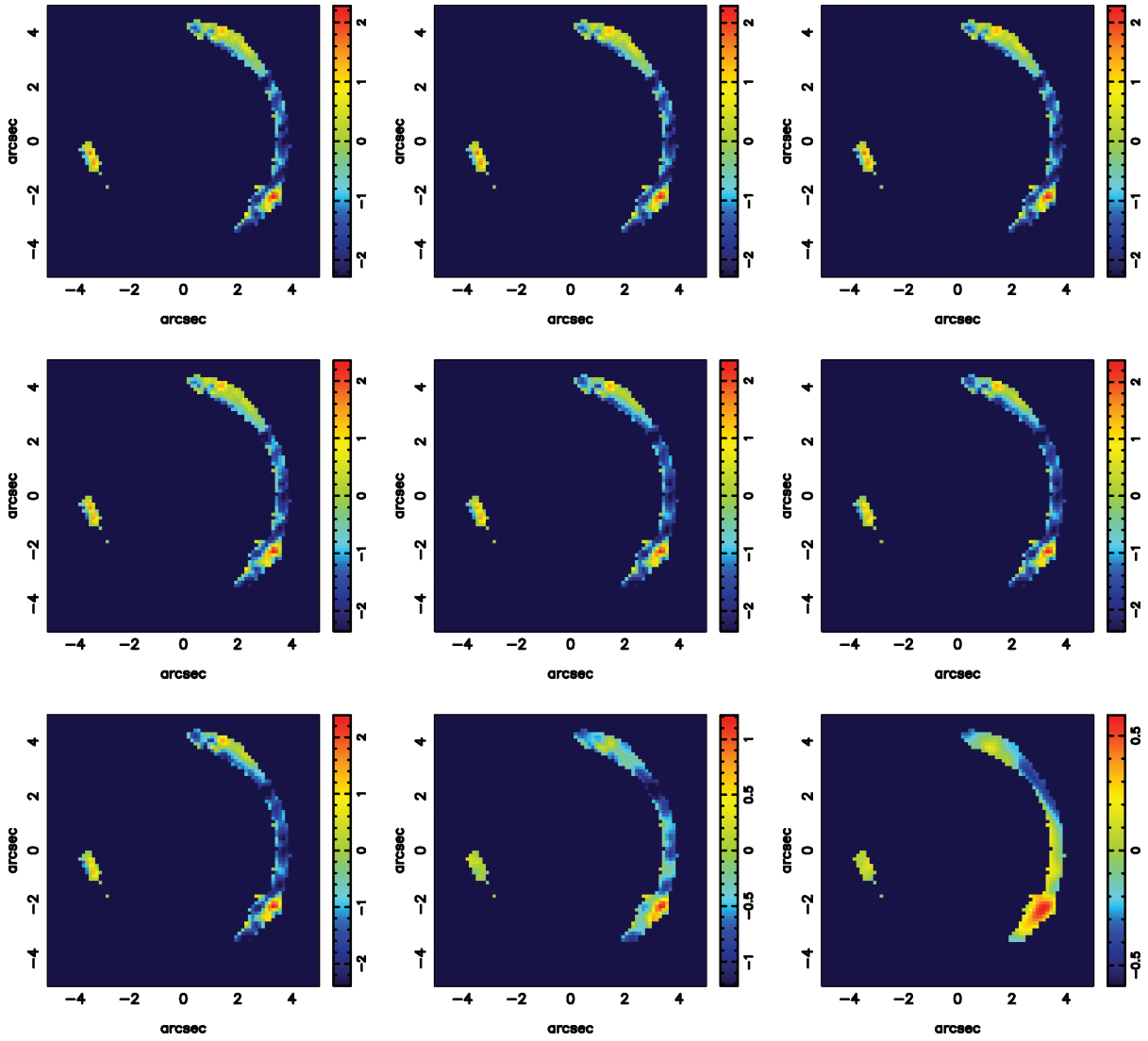

Figure 4. Results of the pixelized reconstruction of the convergence corrections for different values of the source and potential regularization $\lambda_s = 3 \times 10^3$ (top row), $\lambda_s = 3 \times 10^4$ (middle row), $\lambda_s = 3 \times 10^6$ (bottom row) $\lambda_{\delta\psi} = 3 \times 10^7$ (left-hand column) and $\lambda_{\delta\psi} = 3 \times 10^8$ (middle column) and $\lambda_{\delta\psi} = 3 \times 10^9$ (right-hand column).

to a general smooth deviation between the starting mass model and the true mass model. The over-density near the bottom of the arc is positioned exactly where G4 is observed.

Reconstructions with different values of source and potential regularization lead to very similar results (see Fig. 4). As expected, the potential correction at the position of G4 becomes more extended and less concentrated for higher levels of regularizations ($\lambda_s = 3.0 \times 10^6$ and $\lambda_{\delta\psi} = 3.0 \times 10^9$, $\lambda_s = 3.0 \times 10^6$ and $\lambda_{\delta\psi} = 3.0 \times 10^8$) but is otherwise the same for all other combinations of these parameters. This indicates the robustness of the results against changes in the source structure and potential smoothness.

Also the single global SIE leads to a similar convergence map, with the density correction corresponding to G4 located at the same position and having a comparable intensity as for the multiple-component model. The satellite detection is therefore robust against different choices for the initial smooth global lens potential. In fact, an SIE+PJ model is slightly better than a PL+2SIS+PJ one. This could be interpreted as due to the presence of a common halo for this group of galaxies. It is important to note that the convergence correction is located exactly at the position of the peak of the surface brightness distribution of G4 as recovered in Section 2 via a Gaussian fit.

We conclude that the extra freedom allowed to the lens potential via the linear potential corrections compensates/corrects for the inadequacies of the global lens potential and both identify and precisely locate possible mass substructure.

3.3 Satellite mass

In this section, we further quantify the pixelized substructure by an analytic model and constrain the relative parameters in the context of that model. We assume an analytic mass model consisting of a single PL for G1, two SIS for G2, G3 and a pseudo-Jaffe (PJ) for G4 as well as a simplified model SIE+PJ. The PJ profile reads as (e.g. Dalal & Kochanek 2002; Vegetti et al. 2009)

$$\Sigma(r) = \frac{\Sigma_{\rm c} b_{\rm sub}}{2}\left[r^{-1} - \left(r^2 + r_{\rm t}^2\right)^{-1/2}\right], \qquad (2)$$

where $r_t = \sqrt{b_{sub} b}$ is the tidal radius for a lens strength b_{sub}. The satellite G4 is centred on the position where the peak of the convergence correction was found by the pixel-based reconstruction. The free parameters for G1, G2 and G3 are the same as before, while the only free parameter for G4 is the mass within the tidal radius $M_{sub} = \pi r_t b_{sub} \Sigma_c$. The recovered best parameters are listed in Table 1 for both models. The inferred substructure mass is not strongly affected by small changes in the substructure position; a systematic change of 1 pixel in the centre coordinates leads, for example, to a change in the substructure mass of only 1 per cent.

They, respectively, lead to a satellite mass and tidal radius $M_{sub} = (2.78 \pm 0.04) \times 10^{10}\,M_\odot$, $r_t = 0.68$ arcsec (PL+2SIS+PJ) and $M_{sub} = (2.75 \pm 0.04) \times 10^{10}\,M_\odot$, $r_t = 0.81$ arcsec (SIE+PJ).

The reader should not be tempted to compare the different models in terms of the likelihood reported in Table 1; models can formally only be compared in terms of the Bayesian evidence, which requires to integrate over the multidimensional space of the posterior probability density distribution over the free parameters. Whereas this indeed is formally correct, in circumstances where the difference in the maximum a-posteriori probability (MAP) values is substantial, as is the case between models with and without G4 in the mass model (see Table 1), we can omit such an operation. The reason is that the evidence can be approximated by the maximum-likelihood value times the volume over which the likelihood is large (say larger than the prior probability), divided by the volume of the prior space. In the unlikely case of, say, a reduction of a factor of 10^4 in the parameter uncertainty going from the prior to the posterior probability distribution for each of $\leq$17 free parameters, the reduction in volume is $\ln(10^{4\times17}) \approx 160$. Hence conservatively, the difference between the evidence and maximum likelihood values will be $|\ln(\mathcal{E}) - \ln(\mathcal{L})| \lesssim 160$. In practice, the *difference* between evidences for different models will be even smaller because the difference in volume ratios between different models in general is far less than their absolute values. Thus because the difference between the MAP values of the mass models including and excluding G4 is of the order of 5×10^4, respectively, we can safely neglect the difference between maximum likelihood and evidence, even in the case of a difference in degrees of freedom. Consequently, a model comparison in terms of evidence is not relevant for our current analysis and this step is not carried out. Obviously if the difference in evidence between models approaches the difference in degrees of freedom or the volume ratio, this approximation is not valid and a full marginalization is needed (see e.g. Vegetti et al. 2009).

3.4 Satellite mass-to-light ratio

Finally, we estimate the luminosity of G4 by integrating the Gaussian model to the F606W surface brightness profile obtained in Section 2. We expect this to lead to an underestimate of the luminosity, because of the sharply dropping wings of the Gaussian model. Fitting more realistic models is, however, difficult due to the compactness of G4 and the contamination with the arc light. The colour of G4 is consistent with that of the main lens galaxies G1, G2 and G3, which indicates an old stellar population. The absolute rest-frame B-band magnitude is obtained following the prescription of Treu et al. (1999) for an elliptical galaxy and is $M_B = -17.5$, corresponding to a luminosity of $L_B = (1.6 \pm 0.8) \times 10^9\,L_\odot$. The large error estimate includes the uncertainty due to arc light contaminating G4 and the model uncertainty for the light profile. The total mass-to-light ratio of G4, inside the tidal radius, is thus $(M/L)_B = (17.2 \pm 8.5)\,M_\odot/L_\odot$. As explained, this should be really only considered an upper limit to the true mass-to-light ratio. Plausible de Vaucouleur profiles are typically 0.8 mag brighter than the Gaussian model, leading to a total luminosity of $L_B = (3.3 \pm 1.6) \times 10^9\,L_\odot$ and a mass-to-light ratio of $(M/L)_B = (8.2 \pm 4.1)\,M_\odot/L_\odot$. This result is consistent with little to no dark matter inside the tidal radius of this satellite; this is also in agreement with the typical stellar mass-to-light ratio at this redshift $(M/L)_B \approx 5\,M_\odot/L_\odot$ (Treu et al. 2005).

4 SUMMARY

We have applied the grid-based Bayesian lensing code by Vegetti & Koopmans (2009a) to the lens system SDSS J120602.09+514229.5, which has a known luminous satellite located on the lensed arc. We have shown that the perturbation of the lensed arc, created by the satellite, can be used to gravitationally identify the satellite itself and determine its lensing properties, in particular to get an accurate mass measurement. We performed several tests that show that the satellite detection and its recovered mass are robust against changes in the source structure, level of lens potential smoothness and choice of the smooth global lensing model. The main results of this work can be summarized as follows.

(i) A relatively complex model, containing one single PL, two SIS and a PJ satellite, yields a satellite mass $M_{sub} = (2.75 \pm 0.04) \times 10^{10}\,M_\odot$ inside the tidal radius. This result is consistent with a simpler SIE+PJ model.

(ii) The satellite has a total mass-to-light ratio within the tidal radius of $(M/L)_B \approx 8.0\,M_\odot/L_\odot$, consistent with the presence of little to no dark matter inside the tidal radius, assuming a typical stellar $(M/L_B)_\star \approx 5.0\,M_\odot/L_\odot$.

(iii) G1, the main galaxy in the group, has a density profile which is sub-isothermal with slope $\gamma = 1.6 \pm 0.1$. This is not unexpected for galaxies in groups (e.g. Sand et al. 2004).

(iv) We measure for G1 a velocity dispersion of $\sigma_{kinem} = 380 \pm 60\,km\,s^{-1}$ within the SDSS aperture of a diameter of 3 arcsec. This is consistent with the σ_{SIE} value from Lin et al. (2009) obtained by fitting an SIE model to the lens configuration. From a more proper lensing and dynamics model, we predict a stellar velocity dispersion of $340\,km\,s^{-1}$ for the best PL model of G1 that has a logarithmic density slope of $\gamma = 1.6$. Conversely, we predict a density slope of $\gamma = 1.7^{+0.25}_{-0.30}$ (68 per cent CL) from the observed stellar velocity dispersion. This agrees very well with that determined from the PL model of G1, but is also still marginally in agreement with the SIE model.

This paper demonstrates the great potential of pixelized lensing techniques in robustly identifying and measuring the key properties of small mass structure/dwarf satellites in distant galaxies. The application of this method to a large uniform set of lens galaxies will allow us in the near future to constrain the general properties of mass substructure in galaxies and to test the CDM paradigm on these small scales.

ACKNOWLEDGMENTS

SV, OC and LVEK are supported (in part) through an NWO-VIDI programme subsidy (project number 639.042.505). This paper is based on observations made with the NASA/ESA *HST*, obtained at the Space Telescope Science Institute, which is operated by the

Association of Universities for Research in Astronomy, Inc., under NASA contract NAS 5-26555.

REFERENCES

Barnabè M., Nipoti C., Koopmans L. V. E., Vegetti S., Ciotti L., 2009, MNRAS, 393, 1114
Bolton A. S., Burles S., Koopmans L. V. E., Treu T., Moustakas L. A., 2006, ApJ, 638, 703
Czoske O., Barnabè M., Koopmans L. V. E., Treu T., Bolton A. S., 2008, MNRAS, 384, 987
Dalal N., Kochanek C. S., 2002, ApJ, 572, 25
Kauffmann G., White S. D. M., Guiderdoni B., 1993, MNRAS, 264, 201
Klypin A., Kravtsov A. V., Valenzuela O., Prada F., 1999, ApJ, 522, 82
Koopmans L. V. E., Treu T., Bolton A. S., Burles S., Moustakas L. A., 2006, ApJ, 649, 599
Kormann R., Schneider P., Bartelmann M., 1994, A&A, 284, 285
Kravtsov A., 2010, Advances Astron., 2010, 8
Krist J., 1993, in Hanisch R. J., Brissenden R. J. V., Barnes J., eds, ASP Conf. Ser. Vol. 52, Astronomical Data Analysis Software and Systems II. Astron. Soc. Pac., San Francisco, p. 536
Lin H. et al., 2009, ApJ, 699, 1242
Peng C. Y., Ho L. C., Impey C. D., Rix H.-W., 2002, AJ, 124, 266
Sand D. J., Treu T., Smith G. P., Ellis R. S., 2004, ApJ, 604, 88
Springel V. et al., 2008, MNRAS, 391, 1685
Treu T., Stiavelli M., Casertano S., Moller P., Bertin G., 1999, MNRAS, 308, 1037
Treu T. et al., 2005, ApJ, 633, 174
Valdes F., Gupta R., Rose J. A., Singh H. P., Bell D. J., 2004, ApJS, 152, 251
Vegetti S., Koopmans L. V. E., 2009a, MNRAS, 392, 945
Vegetti S., Koopmans L. V. E., 2009b, MNRAS, 400, 1583
Vegetti S., Koopmans L. V. E., Bolton A., Treu T., Gavazzi R., 2009, preprint (arXiv:0910.0760)

This paper has been typeset from a TEX/LATEX file prepared by the author.